Quantum anomalous Hall effect from intertwined moiré bands

https://doi.org/10.1038/s41586-021-04171-1

Received: 5 July 2021

Accepted: 20 October 2021

Published online: 22 December 2021



Check for updates

Tingxin Li^{1,2,6}, Shengwei Jiang^{1,2,6}, Bowen Shen^{1,6}, Yang Zhang^{3,6}, Lizhong Li¹, Zui Tao¹, Trithep Devakul³, Kenji Watanabe⁴, Takashi Taniguchi⁴, Liang Fu³, Jie Shan^{1,5™} & Kin Fai Mak^{1,5}⊠

Electron correlation and topology are two central threads of modern condensed matter physics. Semiconductor moiré materials provide a highly tuneable platform for studies of electron correlation¹⁻¹². Correlation-driven phenomena, including the $Mottinsulator^{2-5}, generalized\ Wigner\ crystals^{2,6,9}, stripe\ phases^{10}\ and\ continuous\ Mott$ transition^{11,12}, have been demonstrated. However, non-trivial band topology has remained unclear. Here we report the observation of a quantum anomalous Hall effect in AB-stacked MoTe₂/WSe₂ moiré heterobilayers. Unlike in the AA-stacked heterobilayers¹¹, an out-of-plane electric field not only controls the bandwidth but also the band topology by intertwining moiré bands centred at different layers. At half band filling, corresponding to one particle per moiré unit cell, we observe quantized Hall resistance, h/e^2 (with h and e denoting the Planck's constant and electron charge, respectively), and vanishing longitudinal resistance at zero magnetic field. The electric-field-induced topological phase transition from a Mott insulator to a quantum anomalous Hall insulator precedes an insulator-to-metal transition. Contrary to most known topological phase transitions¹³, it is not accompanied by a bulk charge gap closure. Our study paves the way for discovery of emergent phenomena arising from the combined influence of strong correlation and topology in semiconductor moiré materials.

Two-dimensional moiré heterostructures of van der Waals materials present a new paradigm for engineering electron correlation, topology and their interplay^{8,14-16}. In graphene materials, the moiré patterns can produce topological bands with valley-contrasting Chern numbers (time-reversal symmetry is preserved at the single-particle level)¹⁴. With sufficiently flat bands, correlation-driven states with broken symmetries are favoured. Orbital ferromagnetism and quantum anomalous Hall (QAH) effects have been reported 17-19 after the initial discovery of superconductivity and correlated insulating states²⁰. However, lattice models are thought to be unsuitable to describe the low-energy physics in twisted bilayer graphene because of the topological nature of the bands¹⁴. By contrast, the moiré bands are topologically trivial in semiconducting transition metal dichalcogenide (TMD) heterobilayers^{1,7}; the low-energy physics is well described by the single-band Hubbard model^{1,7}, provided by the broken inversion symmetry and Ising spin anisotropy in monolayer TMDs. Intertwining two copies of electronic states in twisted TMD homobilayers has been thought to induce non-trivial band topology and realize the long-sought-after Kane-Mele model for interacting quantum particles in a solid-state platform^{21,22}. An abundance of exotic states of matter, including the topological Mott insulators, QAH insulators and chiral spin liquids, has already been predicted²³⁻²⁶. However, non-trivial band topology has not been realized in TMDs to date.

AB-stacked MoTe₂/WSe₂ heterobilayers

In this study, we report an electric-field-induced topological phase transition from a Mott insulator to a OAH insulator in near-60-degree-twisted (or AB-stacked) MoTe₂/WSe₂ heterobilayers. The two TMDs form a triangular moiré superlattice with three high-symmetry stacking sites: MM, MX and XX (M = Mo or W; X = Te or Se) (Fig. 1a). The lattice mismatch between the two materials is about 7%, giving rise to a moiré lattice period of approximately 5 nm and a moiré density of $n_{\rm M} \approx 5 \times 10^{12} \, {\rm cm}^{-2}$ (ref. 11). In each monolayer, the band edges are located at the K or K' point of the Brillouin zone with twofold coupled spin-valley degeneracy^{1,21}. The heterobilayer has a type-I band alignment with both conduction and valence band edges from MoTe₂, and a valence band offset of 200-300 meV (ref. 11). The application of an out-of-plane electric field can reduce the band offset and tune the moiré band structure because interlayer tunnelling contributes substantially to the formation of the moiré potential. We have recently reported a continuous bandwidth-tuned Mott transition in near-0-degree-twisted (or AA-stacked) MoTe₂/WSe₂ at fixed filling of one hole per moiré unit cell $(v=1)^{11}$. We did not observe any topological phase transitions there. Important distinctions between the two stacking orders include different high-symmetry stacking sites and interlayer spin alignment²⁷; the latter strongly influences interlayer tunnelling and the moiré band structure (Methods).

School of Applied and Engineering Physics and Laboratory of Atomic and Solid State Physics, Cornell University, Ithaca, NY, USA. 2Key Laboratory of Artificial Structures and Quantum Control (Ministry of Education), School of Physics and Astronomy, Shanghai Jiao Tong University, Shanghai, China, 3Department of Physics, Massachusetts Institute of Technology, Cambridge, MA. USA. 4National Institute for Materials Science, Tsukuba, Japan. 5Kavli Institute at Cornell for Nanoscale Science, Ithaca, NY, USA. 6These authors contributed equally: Tingxin Li, Shengwei Jiang, Bowen Shen, Yang Zhang. [™]e-mail: jie.shan@cornell.edu; kinfai.mak@cornell.edu

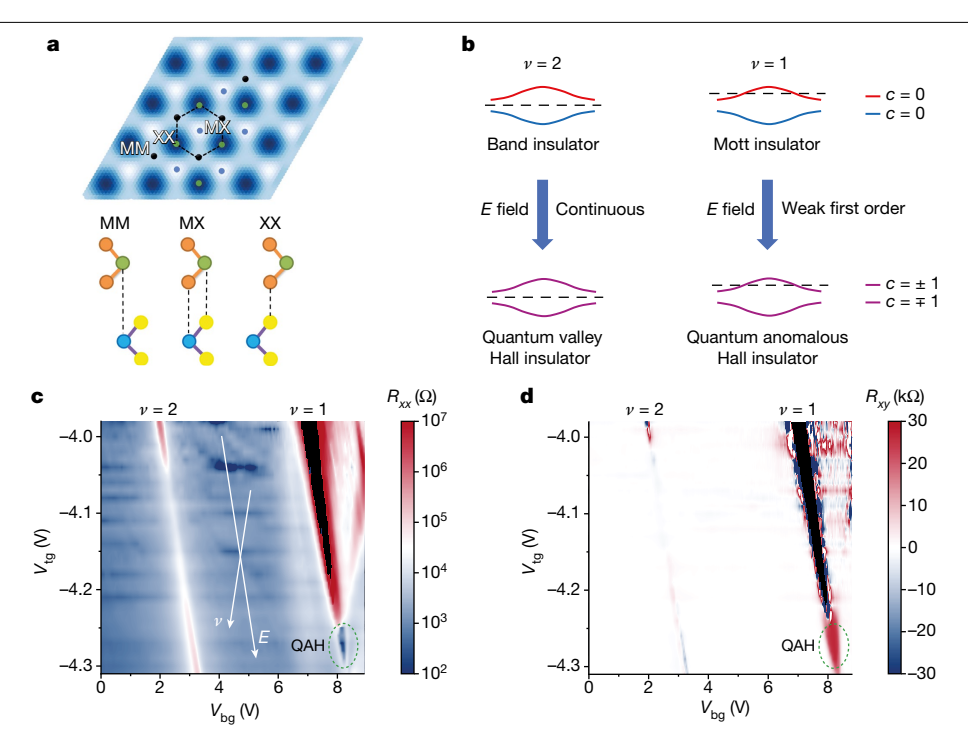


Figure 1 | **AB-stacked MoTe₂/WSe₂ heterobilayer. a**, Top, triangular moiré superlattice with high-symmetry stacking sites MM, MX and XX (M = Mo or W; X = Se or Te). The interlayer distance increases from the white to the blue region. MM and XX form a honeycomb structure (dashed line). Bottom, orange and yellow balls denote X atoms; green and blue balls denote M atoms; dashed lines show vertical atomic alignment. b, Schematic illustration of electric-field-induced topological phase transitions. Topological moiré bands with valley contrasting Chern numbers ($c = \pm 1$) emerge after band inversion. A band insulator–topological insulator transition is expected for the Fermi

level (dashed line) in the gap (v=2). A Mott–QAH insulator transition is also possible for half filling of the first moiré band (v=1) in the strong correlation limit. \mathbf{c} , \mathbf{d} , Longitudinal (\mathbf{c}) and Hall (\mathbf{d}) resistance at 300 mK as a function of top and bottom gate voltages. R_{xx} is measured under zero magnetic field; R_{xy} is the antisymmetrized result under an out-of-plane magnetic field of ± 0.1 T. The two gate voltages vary the filling factor (v) and electric field (E) independently along the white arrow directions. The dashed circles mark the region of a QAH insulator. The black regions are very insulating and experimentally inaccessible.

We perform magneto-transport measurements on dual-gated Hall bar devices of AB-stacked MoTe₂/WSe₂ heterobilayers down to 300 mK (Methods). Figure 1c, d shows, respectively, the longitudinal resistance (R_{xx}) and the Hall resistance (R_{xy}) of device 1 in the zero magnetic field limit as a function of top gate voltage (V_{tg}) and bottom gate voltage $(V_{\rm bg})$ at 300 mK. The two gate voltages independently tune the filling factor (ν) and the vertical electric field $(E \equiv \frac{1}{2}(\frac{V_{\rm bg}}{d_{\rm bg}} - \frac{V_{\rm tg}}{d_{\rm tg}})$, with $d_{\rm tg}$ and $d_{\rm bg}$ denoting the thickness of the top and bottom gate dielectrics, respectively). Extended Data Figure 2 shows the resistances as a function of ν and E. At small E, we observe two prominent resistance peaks at $\nu = 1$ and v = 2, corresponding to the Mott and the single-particle moiré band insulating states, respectively. As E increases, R_{xx} of both states drops by orders of magnitude. These behaviours are similar to that observed in the AA-stacked devices¹¹. However, there is a peculiar region at large electric fields at v = 1 (marked by the dashed circle), in which R_{xx} is down to $1 k\Omega$ or less. This region is absent in the AA-stacked devices. Concomitantly, the region exhibits large Hall resistance close to 26 k Ω (Fig. 1d). This signals the emergence of a new state with broken timereversal symmetry.

Quantum anomalous Hall effect at v = 1

We characterize the state in depth in Fig. 2 by choosing one point from the region in Fig. 1c with minimum R_{xx} (additional data at other points can be found in Extended Data Figs. 4 and 5). Figure 2a, b shows R_{xy} and R_{xx} , respectively, as a function of out-of-plane magnetic field at a temperature ranging from 300 mK to 8 K. At low temperatures, we observe sharp magnetic hysteresis with coercive field around 10 mT. At zero magnetic field, the Hall resistance ($R_{xy} \approx 26 \text{ k}\Omega$) is nearly quantized at h/e^2 and the longitudinal resistance ($R_{xx} \approx 1.3 \text{ k}\Omega$) is substantially smaller

 $(h/e^2 \approx 25.8 \, \mathrm{k}\,\Omega)$ is the resistance quantum). As temperature increases, we observe both a suppression of hysteresis and a departure from resistance quantization in R_{xy} . This is accompanied by a rapid increase in R_{xx} , which also exhibits negative magnetoresistance. By 8 K the hysteresis vanishes; R_{xy} depends linearly on magnetic field and R_{xx} becomes nearly field independent. We summarize the temperature dependence of the zero-field magnitude of R_{xy} and R_{xx} in Fig. 2c to better identify the phase transition. In particular, the Hall resistance remains quantized up to about 2.5 K, and it stays finite up to 5–6 K (the Curie temperature for magnetic ordering).

These observations are distinctive experimental signatures of the QAH effect $^{28-31}$. The slight imperfection (in both R_{xy} quantization and residual R_{xx}) arises presumably from remnant dissipation in the bulk and spatial inhomogeneity of the sample that leads to spatially non-uniform gate voltages required to induce the QAH state. Such inhomogeneity can give rise to QAH and non-QAH puddles and percolation transport to destroy perfect Hall quantization. The transition temperatures in AB-stacked MoTe₂/WSe₂ for both resistance quantization and magnetic ordering are comparable to that in twisted bilayer graphene¹⁷. The QAH effect here is robust and reproducible. We have studied a total of five devices. All show similar behaviours: three devices exhibit the QAH effect at v=1 (Extended Data Fig. 3); the remainder of the devices show quantized Hall resistance under a moderate magnetic field of about 1T, which is probably due to higher levels of sample inhomogeneity.

The electrical transport of the QAH insulator is dominated by chiral edge states³¹. It possesses non-trivial band topology with a total Chern number of occupied bands, |c| = 1, inferred from the quantized Hall resistance $(R_{xy} = \frac{1}{|c|} \frac{e^2}{e^2})$. This is further verified by studying the dispersion of the state in doping density and magnetic field and invoking the Streda formula, which relates the Hall resistance to the derivative of

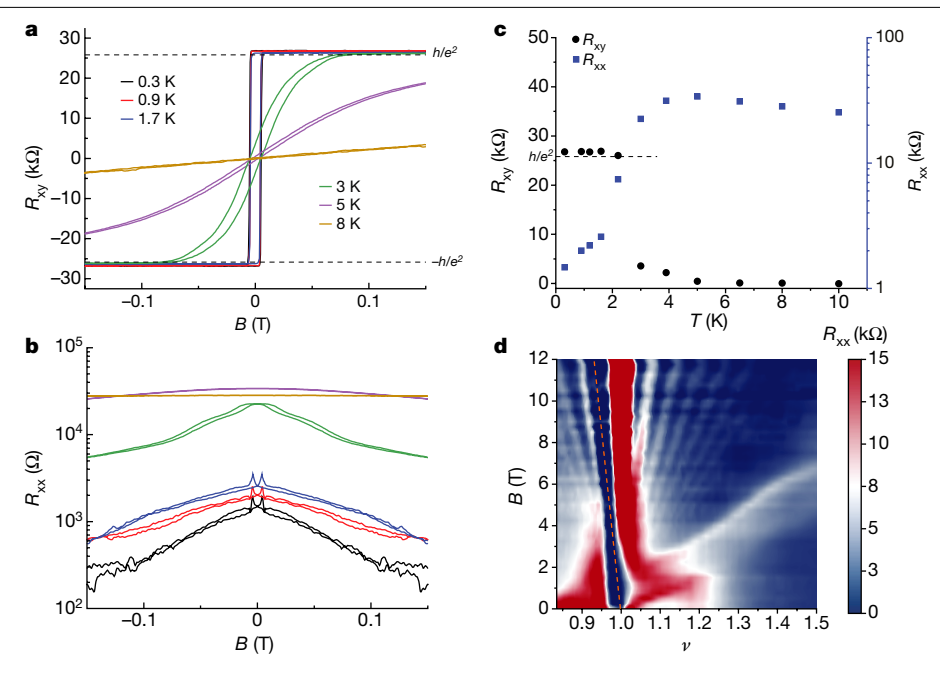


Figure 2 | Quantized anomalous Hall effect at v = 1.a, b, Magnetic-field dependence of $R_{xy}(\mathbf{a})$ and $R_{xx}(\mathbf{b})$ of the QAH insulator at varying temperatures. Quantized Hall resistance $(R_{xy} \approx \frac{h}{e^2})$ and small longitudinal resistance $(R_{xx} \ll R_{xy})$, accompanied by a negative magnetoresistance, are observed at the three lowest temperatures. There is also a clear magnetic hysteresis with a sharp magnetic switching near ±10 mT. c, Temperature dependence of the

zero-magnetic-field values of R_{xy} and R_{xx} . The onset of magnetic ordering is at approximately 5-6 K and quantization of R_{xy} happens below approximately 2.5 K. The dependences of R_{xy} and R_{xx} are perfectly correlated. **d**, R_{xx} as a function of magnetic field and filling factor at 300 mK. The filling of the R_{xx} minimum (dashed line) disperses with magnetic field with a slope corresponding to Chern number -1.

doping density with respect to magnetic field³². Figure 2d shows R_{xx} as a function of density ν (in units of $n_{\rm M}$) and magnetic field B at 300 mK. We identify the QAH state by the resistance minimum growing out of B = 0 and v = 1 (dashed line) and determine $c = \frac{h}{e} \frac{dv}{dB} n_M = -0.95 \pm 0.05$ from the slope of the dashed line. (A Landau fan with level degeneracy of 1 is also observed to emerge from v = 1 above 3 T.) The result is fully consistent with the quantized Hall resistance.

Mott-to-QAH quantum phase transition

Next, we examine the transition from the topologically trivial Mott insulator to the topologically non-trivial QAH insulator at v = 1. Figure 3a shows the electric-field dependence of R_{xx} under zero magnetic field for varying temperatures. No hysteresis is observed down to 300 mK (Extended Data Fig. 4). We identify three distinctive regions for E. The temperature dependence of R_{xx} for one representative electric field from each region is shown in Fig. 3b. For small E (shaded in orange in Fig. 3a), we observe large R_{xx} which diverges rapidly as temperature decreases. This is the Mott insulating state, in agreement with a previous study¹¹. At large E (shaded in pink Fig. 3a), resistance drops to about 10 k Ω at the highest E available in this study; it weakly depends on temperature and is finite in the zero-temperature limit. This corresponds to a metallic behaviour; further investigations are required to understand the nature of this metallic state. In the middle region (shaded in blue Fig. 3a), R_{xx} exhibits an insulating behaviour above approximately 5 K, below which it drops rapidly as the QAH insulator is stabilized and transport is dominated by the chiral edge states. These results show that the Mott-to-QAH insulator transition precedes the insulator-to-metal transition.

We determine the charge gap energy of different phases by performing electronic compressibility measurements³³ (Methods), which can assess the bulk charge gap across the topological phase transition without the influence of the chiral edge states. Figure 3d shows the gate voltage dependence of the differential capacitance, C, between

the top gate electrode and the sample at 300 mK and zero magnetic field (device 6). The capacitance is normalized by the geometrical capacitance, $C_{\rm g}$, defined by the sample–gate distance and the dielectric constant of the gate dielectrics. The capacitance map resembles that of R_{xx} (Fig. 1c for device 1), minus the signature of the QAH state because compressibility is not affected by edge transport. We observe that $C/C_{\sigma} \approx 0$ when the sample is charge neutral (not shown) and $C/C_{\sigma} \approx 1$ when the sample is heavily doped and behaves like a metallic plate³⁴. The dips in C/C_g at finite filling factors correspond to incompressible/ insulating states. The charge gap can be evaluated by integrating the dip area³⁴. The charge gap at v = 1 is shown in Fig. 3c (blue squares). It decreases monotonically as *E* increases.

We identify the QAH region (shaded in blue in Fig. 3a and 3c) by its characteristic dispersion in doping density and magnetic field as in Fig. 2d (Methods and Extended Data Fig. 7; the Hall resistance measurement is not compatible with this device). The electric-field span for the QAH state (approximately 10 mV nm⁻¹) is similar to that in other devices. Within our experimental resolution, we do not observe any bulk charge gap closure across the Mott-to-QAH insulator transition (see Extended Data Fig. 7e for further evidence). This is further supported by the charge gap from an activation fit of the temperature dependence of the resistance of device 1 (orange circles in Fig. 3c) (see Extended Data Fig. 6 for analysis). The charge gaps from two different devices are also largely consistent after aligning the critical field for either the Mott-to-QAH or the QAH-to-metal boundary.

Band inversion at v = 2

Next, we propose a mechanism for the observed QAH state in ABstacked MoTe₂ /WSe₂ heterobilayers. We characterize the moiré bands and the associated wave functions by density functional theory calculations (Methods and Extended Data Figs. 8 and 9). The wave functions of the first and second dispersive moiré valence bands

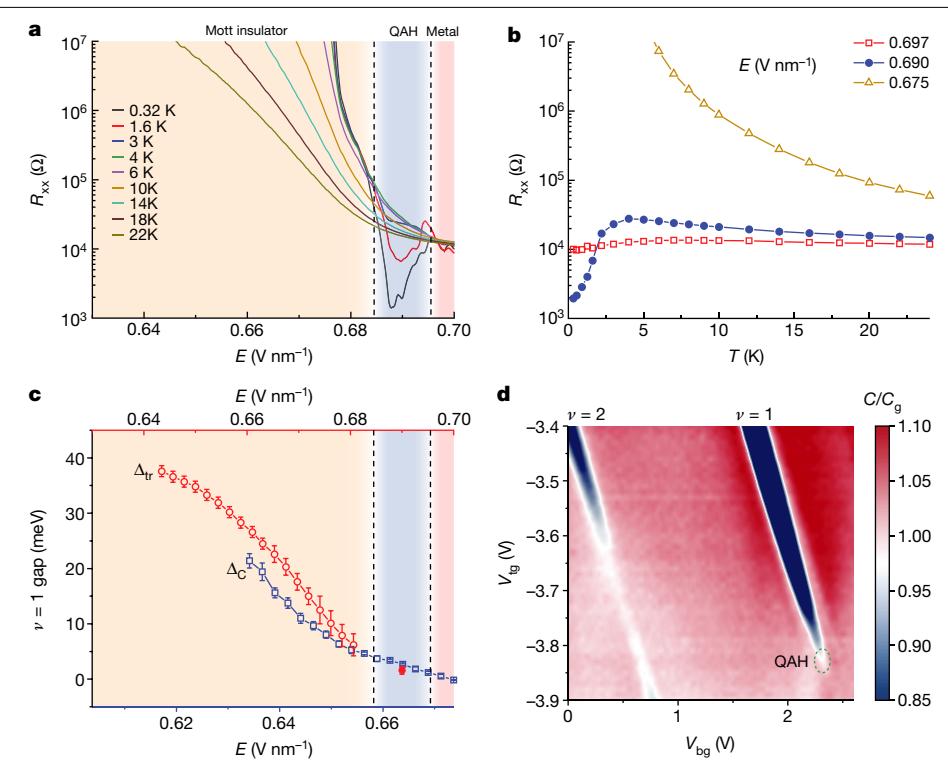


Figure 3 | **Mott–QAH insulator transition at v** = **1.a**, Electric-field dependence of R_{xx} at v=1 under zero magnetic field at varying temperatures (device 1). Three regions, corresponding to a Mott insulator, QAH insulator and metal, are identified. **b**, Representative temperature dependences of R_{xx} , one from each region. **c**, Charge gap as a function of electric field extracted from thermal activation transport (red circles, device 1, top axis) and extracted from capacitance measurements at 300 mK (blue squares, device 6, bottom axis). The error bars for the red symbols are uncertainties of the activation fit; the error bars for the blue symbols are propagated uncertainties of the

capacitance measurement and numerical integration of the capacitance dips. The two electric-field axes are slightly shifted to match the phase boundaries in the two devices. The charge gap evolves smoothly across the topological phase transition. ${\bf d}$, Differential top-gate capacitance at 300 mK and zero magnetic field as a function of gate voltages (device 6). The two prominent incompressible states correspond to v=1 and v=2. The green dashed line denotes the QAH region, identified by the magnetic-field dispersion of the state (Extended Data Fig. 7). The lines in ${\bf a}$ and ${\bf c}$ are guides to the eye.

initially reside primarily on the MoTe₂ and WSe₂ layers, respectively. They are also centred at two different sites of the moiré unit cell (MM and XX, respectively) to form a honeycomb lattice structure (Fig. 1a). The out-of-plane electric field tunes the potential difference between the two sites. The moiré band gap at the K_m or K_m' point of the moiré Brillouin zone closes and reopens as E increases. A non-zero valley-contrasting Chern number is developed for the bands after the gap reopens (Fig. 1b). The physics of the first two moiré bands therefore resembles the Kane-Mele model in the presence of a staggered $sublattice\ potential^{13}.\ This\ is\ similar\ to\ the\ case\ of\ twisted\ TMD\ homology and the case of\ twisted\ tw$ bilayers with $E \approx 0$ (refs. ^{21,22}). In this model, the v = 2 state after gap reopening is a quantum valley-spin Hall insulator, which hosts helical edge states. At v = 1, strong electron correlation can spontaneously break time-reversal symmetry and stabilize a QAH insulator^{21,22,35}. The two topological phase transitions, however, do not necessarily occur at the same electric field (Methods).

The proposed picture is supported by the behaviour of the v=2 state in our experiment. The electric-field dependence of R_{xx} at varying temperatures (Fig. 4a) shows a charge gap minimum; the state is insulating on both sides of the minimum. This is consistent with the charge gap determined from the compressibility measurements at 300 mK (Fig. 4b). The results indicate that the moiré band gap closes and reopens as E increases (the small non-zero gap near the critical point is presumably from disorder broadening of the transition and/or the emergence of an excitonic insulating state for a small gap insulator). We also observe large magnetoresistance immediately after gap closure under an in-plane magnetic field (Fig. 4c, d), but weak magnetoresistance (approximately 10% at 0.5 T) on both sides of the

critical point under an out-of-plane magnetic field. The behaviour is compatible with that of a quantum valley-spin Hall insulator after gap closure 13 . The counter-propagating helical edge states are expected to possess Ising-like spins as in monolayer TMDs; thus only an in-plane magnetic field can mix them to enhance backscattering and induce large magnetoresistance 36 . The presence of a helical edge state is also supported by the non-local transport study in Extended Data Fig. 10. The resistance is, however, substantially larger than $\hbar/2e^2$ because of backscattering in the helical edge states and bulk dissipation due to the small charge gap.

Additional discussion and conclusion

We note the very unusual absence of bulk gap closure at the Mott-to-QAH insulator transition observed at v=1. The commonly known topological phase transitions involve closing and reopening of a charge gap^{13,23}, such as the continuous transition at v=2. A topological phase transition without charge gap closure is, however, allowed if the two phases involved have different symmetries^{22,23,37,38}. The QAH insulator here is probably valley polarized^{21,22,35}. The Mott insulator could be non-magnetic³⁹ or with 120-degree Néel order¹. In the former, time-reversal symmetry is broken only in the QAH insulator. In the latter, the valley pseudospin evolves from a non-collinear to a collinear state. In principle, both scenarios allow a topological phase transition without charge gap closure. Because the QAH insulator has chiral edge states, the transition is probably a weak first-order transition with a small gap discontinuity, which could be smeared out by disorder broadening in our devices.

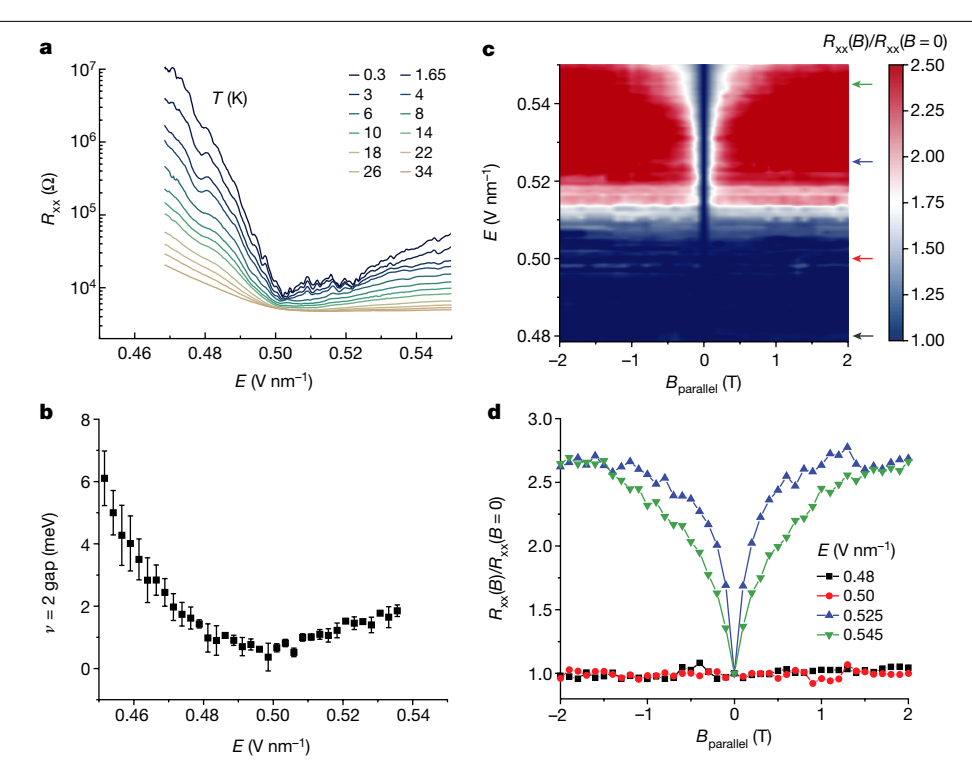


Figure 4 | Evidence of a quantum valley-spin Hall insulator at v = 2. a, Electric-field dependence of R_{xx} at v = 2 under zero magnetic field for varying temperatures (device 1). The temperature dependence is much weaker after gap reopening. **b**, Charge gap at v = 2 from capacitance measurements at 300 mK (device 6). As electric field increases, the charge gap closes and reopens. The gap size is much smaller after gap reopening. The error bars are

propagated uncertainties of the capacitance measurement and numerical integration of the capacitance dips. c, Electric-field dependence of magnetoresistance, $R_{xx}(B)/R_{xx}(B=0)$, under an in-plane magnetic field at 300 mK. d, Magnetoresistance (symbols) at selected electric fields denoted by arrows in c. The lines are guides to the eye. Strong magnetoresistance is observed only after gap reopening.

In conclusion, we have observed a topological phase transition from a Mott insulator to a QAH insulator in AB-stacked MoTe₂/WSe₂ heterobilayers at v = 1. The transition does not exhibit any sign of charge gap closure and is probably a weak first-order transition. It is correlated with a continuous topological phase transition from a moiré band insulator to a possible quantum valley-spin Hall insulator at v = 2. Future studies are required to verify the nature of the v = 2 state after gap closure, as well as the valley-polarized nature of the observed OAH insulator. Our results establish semiconductor moiré materials as a versatile system for exploring the phenomenology involving electronic correlation and topology.

Online content

Any methods, additional references, Nature Research reporting summaries, source data, extended data, supplementary information, acknowledgements, peer review information; details of author contributions and competing interests; and statements of data and code availability are available at https://doi.org/10.1038/s41586-021-04171-1.

- Wu, F., Lovorn, T., Tutuc, E. & MacDonald, A. H. Hubbard model physics in transition metal 1. dichalcogenide moiré bands, Phys. Rev. Lett. 121, 026402 (2018).
- 2. Regan, E. C. et al. Mott and generalized Wigner crystal states in WSe₂/WS₂ moiré superlattices, Nature 579, 359-363 (2020).
- Tang, Y. et al. Simulation of Hubbard model physics in WSe₂/WS₂ moiré superlattices. 3. Nature 579, 353-358 (2020).
- Wang, L. et al. Correlated electronic phases in twisted bilayer transition metal dichalcogenides. Nat. Mater. 19, 861-866 (2020).
- 5 Shimazaki, Y. et al. Strongly correlated electrons and hybrid excitons in a moiré heterostructure. Nature 580, 472-477 (2020).
- Xu, Y. et al. Correlated insulating states at fractional fillings of moiré superlattices. Nature 6 587, 214-218 (2020)
- 7. Zhang, Y., Yuan, N. F. Q. & Fu, L. Moiré quantum chemistry: charge transfer in transition metal dichalcogenide superlattices. Phys. Rev. B 102, 201115 (2020).

- Andrei, E. Y. et al. The marvels of moiré materials. Nat. Rev. Mater. 6, 201-206 (2021)
- Huang, X. et al. Correlated insulating states at fractional fillings of the WS₂/WSe₂ moiré lattice, Nat. Phys. 17, 715-719 (2021)
- Jin, C. et al. Stripe phases in WSe₃/WS₃ moiré superlattices. Nat. Mater. 20, 940-944 (2021)
- 11. Li. T. et al. Continuous Mott transition in semiconductor moiré superlattices. Nature 597. 350-354 (2021).
- Ghiotto, A. et al. Quantum criticality in twisted transition metal dichalcogenides. Nature **597**, 345-349 (2021).
- Hasan, M. Z. & Kane, C. L. Colloquium: topological insulators. Rev. Mod. Phys. 82, 3045-3067 (2010)
- Andrei, E. Y. & MacDonald, A. H. Graphene bilayers with a twist. Nat. Mater. 19, 1265-1275 (2020)
- 15. Balents, L., Dean, C. R., Efetov, D. K. & Young, A. F. Superconductivity and strong correlations in moiré flat bands. Nat. Phys. 16, 725-733 (2020).
- Kennes, D. M. et al. Moiré heterostructures as a condensed-matter quantum simulator. Nat. Phys. 17, 155-163 (2021).
- Serlin, M. et al. Intrinsic quantized anomalous Hall effect in a moiré heterostructure. Science 367, 900-903 (2020).
- Sharpe, A. L. et al. Emergent ferromagnetism near three-quarters filling in twisted bilayer graphene. Science 365, 605-608 (2019).
- Chen, G. et al. Tunable correlated Chern insulator and ferromagnetism in a moiré superlattice. Nature 579, 56-61 (2020).
- 20. Cao, Y. et al. Unconventional superconductivity in magic-angle graphene superlattices. Nature 556, 43-50 (2018).
- Wu, F., Lovorn, T., Tutuc, E., Martin, I. & MacDonald, A. H. Topological insulators in twisted transition metal dichalcogenide homobilayers, Phys. Rev. Lett. 122, 086402 (2019).
- 22 Devakul, T., Crépel, V., Zhang, Y. and Fu, L. Magic in twisted transition metal dichalcogenide bilayers. Nat. Commun. https://doi.org/10.1038/s41467-021-27042-9 (2021).
- 23. Hohenadler, M. & Assaad, F. F. Correlation effects in two-dimensional topological insulators. J. Phys. Condens. Matter 25, 143201 (2013).
- Witczak-Krempa, W., Chen, G., Kim, Y. B. & Balents, L. Correlated quantum phenomena in the strong spin-orbit regime. Annu. Rev. Condens. Matter Phys. 5, 57-82 (2014).
- 25. Pesin, D. & Balents, L. Mott physics and band topology in materials with strong spin-orbit interaction. Nat. Phys. 6, 376-381 (2010).
- Raghu, S., Qi, X.-L., Honerkamp, C. & Zhang, S.-C. Topological Mott insulators. Phys. Rev. Lett. 100, 156401 (2008)
- Zhang, Y., Devakul, T. & Fu, L. Spin-textured Chern bands in AB-stacked transition metal dichalcogenide bilayers. Proc. Natl Acad. Sci. USA 118, e2112673118 (2021).

- Chang, C.-Z. et al. Experimental observation of the quantum anomalous Hall effect in a magnetic topological insulator. Science 340, 167-170 (2013).
- Kou, X. et al. Scale-invariant quantum anomalous Hall effect in magnetic topological insulators beyond the two-dimensional limit. Phys. Rev. Lett. 113, 137201
- 30. Mogi, M. et al. Magnetic modulation doping in topological insulators toward higher-temperature quantum anomalous Hall effect. Appl. Phys. Lett. 107, 182401
- 31. Liu, C.-X., Zhang, S.-C. & Qi, X.-L. The quantum anomalous Hall effect: theory and experiment. Annu. Rev. Condens. Matter Phys. 7, 301-321 (2016).
- 32. MacDonald, A. H. Introduction to the physics of the quantum Hall regime. Preprint at arXiv:cond-mat/9410047 (1994).
- Young, A. F. et al. Tunable symmetry breaking and helical edge transport in a graphene quantum spin Hall state. Nature 505, 528-532 (2014).
- 34. Li, T. et al. Charge-order-enhanced capacitance in semiconductor moiré superlattices. Nat. Nanotechnol. 16, 1068-1072 (2021).

- 35. Y. M. Xie, C. P. Zhang, J. X. Hu, K. F. Mak & Law, K. T. Theory of valley polarized quantum anomalous Hall state in moiré $MoTe_2/WSe_2$ heterobilayers. Preprint at arXiv:2106.13991 (2021).
- 36. Fei, Z. et al. Edge conduction in monolayer WTe₂. Nat. Phys. 13, 677-682 (2017).
- 37. Amaricci, A., Budich, J. C., Capone, M., Trauzettel, B. & Sangiovanni, G. First-order character and observable signatures of topological quantum phase transitions. Phys. Rev. Lett. 114, 185701 (2015).
- 38. Ezawa, M., Tanaka, Y. & Nagaosa, N. Topological phase transition without gap closing. Sci. Rep. 3, 2790 (2013).
- Senthil, T. Theory of a continuous Mott transition in two dimensions. Phys. Rev. B 78, 045109 (2008).

Publisher's note Springer Nature remains neutral with regard to jurisdictional claims in published maps and institutional affiliations.

© The Author(s), under exclusive licence to Springer Nature Limited 2021

Methods

Device fabrications

We fabricated 60-degree-aligned MoTe₂/WSe₂ Hall bar devices (Extended Data Fig. 1) using the layer-by-layer dry transfer method as detailed in refs. 11,40. In brief, we exfoliated the constituent atomically thin flakes from bulk crystals (HQ Graphene) and picked them up sequentially using a polymer stamp to form the desired stack. The crystal orientations of WSe₂ and MoTe₂ monolayers and the twist angle between them were determined by angle-resolved optical second-harmonic generation spectroscopy^{2,3}. The angle alignment accuracy is typically ±0.5°. We used 5-nm-thick Pt as metal electrodes to achieve good electrical contacts to the sample while keeping the strain effects minimal. We also used a relatively thin (approximately 5 nm) hexagonal boron nitride (hBN) layer as the top gate dielectric to achieve a large breakdown electric field of approximately 1 V nm⁻¹. We fabricated the capacitance devices following the design reported in ref. 34. To achieve good electrical contacts to the sample, one of the gates covers the entire heterobilayer and creates a heavily hole-doped contact region. The other gate depletes the hole density in the region of interest for resistance and capacitance measurements. Good electrical contacts can be achieved for a limited range of high electric fields for the transport and capacitance studies. However, strong electric-field dependence is not expected at small electric fields as, with large interlayer band offset, the low-energy physics in the heterobilayers is well captured by the single-band Hubbard model in the limit of strong interaction^{1-3,6}. The typical contact resistance in the QAH region is approximately $100-200 \text{ k}\Omega$. We have studied a total of five Hall bar devices. Three devices show the quantized anomalous Hall effect near zero magnetic field at v = 1. The results for device 1 are presented in the main text. The results for devices 2 and 3 are shown in Extended Data Fig. 3.

Electrical transport measurements

The electrical transport measurements were performed in a closed-cycle 4 He cryostat (Oxford TeslatronPT) equipped with a superconducting magnet and a 3 He insert (base temperature about 300 mK). Low-frequency (<23 Hz) lock-in techniques were used to measure the sample resistance under a small bias voltage of 1–2 mV to avoid sample heating. The bias current was kept below 15 nA while probing the QAH insulator. Both the voltage drop at the probe electrode pairs and the source-drain current were recorded. Voltage pre-amplifiers with large input impedance (100 M Ω) were used to measure the sample resistance up to about 10 M Ω . Finite longitudinal-transverse coupling occurs in our devices that mixes R_{xx} and R_{xy} . To correct this effect, we used the standard procedure to symmetrize ($\frac{R_{xx}(B) + R_{xx}(-B)}{2}$) and antisymmetrize ($\frac{R_{xy}(B) - R_{xy}(-B)}{2}$) the measured R_{xx} and R_{xy} under positive and negative magnetic fields to obtain accurate values of R_{xx} and R_{xy} , respectively.

$Electron\,quantum\,coherence\,time$

We estimate the electron coherence time τ using the magnetic field $B_0 \sim 2$ T that corresponds to the onset of quantum oscillations in our devices (Fig. 2d), $\omega_c \tau = \frac{eB_0 \tau}{m} \sim 1$. Here ω_c is the cyclotron frequency and the band mass m is assumed to take the value of the free electron mass m_0 . The disorder energy level broadening is estimated to be $\hbar/\tau \sim 0.2$ meV This value corresponds to a quantum electron mobility of about 5,000 cm² V⁻¹ s⁻¹. The disorder energy level broadening is about an order of magnitude smaller than the QAH gap size of approximately 2 meV.

Capacitance measurements

The capacitance measurements were performed in the same cryostat as the electrical transport measurements. Details have been reported in a recent study of $MoSe_2/WS_2$ heterobilayers³⁴. In comparison, $MoTe_2/WSe_2$ heterobilayers have substantially lower electrical contact resistance; the differential capacitance can be measured at lower

temperatures and over a larger frequency range. We used a commercial high electron mobility transistor (model FHX35X), which is connected to the sample on the same chip as a first-stage amplifier 41,42 ; it effectively decouples the device capacitance from the parasitic capacitance due to the cabling. We measured the differential top-gate capacitance, C, by applying an a.c. voltage (10 mV in amplitude and 3–5 kHz in frequency) to the heterobilayer and collecting charges from the top gate through the high electron mobility transistor by lock-in techniques. The top-gate capacitance C is related to the quantum capacitance, C_Q , of the heterobilayer by $\frac{1}{C} = \frac{1}{C_Q} \left(1 + \frac{C_D}{C_1}\right) + \frac{1}{C_t} \approx \frac{2}{C_Q} + \frac{1}{C_g}$. Here $C_t \approx C_D$ ($\equiv C_Q$) are the geometrical top-gate and back-gate capacitances, respectively, as the two gates are nearly symmetric in the capacitance device (device 6). The chemical potential jump, $\Delta\mu$, at an insulating state can be obtained as $\Delta\mu = e \int dV_t \frac{C_1 - C}{C_1 + C_1 + C_2} \approx \frac{e}{C_2} \int dV_t \left(1 - \frac{C}{C_g}\right)$, where the integration with respect to the top-gate voltage V_t spans the range of the capacitance dip corresponding to the insulating state.

Determination of phase boundaries in capacitance devices

The QAH region can be identified unambiguously using the Streda formula and dispersion of the QAH state in the filling factor—magnetic field map (Extended Data Fig. 7) even though the Hall response is not accessible in capacitance devices. Only the QAH state disperses in this map with the expected slope determined by the Chern number (which is equal to -1). The Mott state shows no dispersion because it is non-topological. This helps to identify the Mott–QAH phase boundary. In addition, when the charge gap closes, the capacitance reaches $C/C_{\rm g} \approx 1$ (Extended Data Fig. 7e). This helps to identify the QAH–metal phase boundary.

Different critical electric fields for topological phase transitions at v = 1 and v = 2

In our devices, the phase transition at $\nu=2$ is observed at a smaller electric field than at $\nu=1$. The two phase transitions are not expected to occur at the same electric field. Although in general the bands are required to be topological for the QAH states to emerge at $\nu=1$, there is no guarantee that the Mott state transitions to the QAH state as soon as the single-particle bands become topological. The topological phase transition at $\nu=1$ is dominated by the electronic correlation effect. The critical field is determined by the ground-state energy of the different competing states ^{22,43}. On the one hand, weaker correlation at higher electric fields does not favour the QAH state. On the other hand, stronger correlation at lower electric fields may favour the Mott state. The emergence of the QAH state may require a fine balance between the competition with the Mott state and with the metallic state.

Band structure calculations and discussions

Density functional theory (DFT) calculations were performed using a generalized gradient approximation 44 with the SCAN+rVV10 van der Waals density functional 45 , as implemented in the Vienna Ab initio Simulation Package 46 . Pseudopotentials were used to describe the electronion interactions. The structure of 60-degree-twisted (or AB-stacked) MoTe $_2$ /WSe $_2$ heterobilayers was constructed using a vacuum spacing of more than 20 Å to avoid artificial interactions between the periodic images in the out-of-plane direction. Structural relaxation was performed on each atom with a force less than 0.01 eV/Å. We used Γ -point sampling for structural relaxation and self-consistent calculations. The relaxed structure is shown in Extended Data Fig. 8. There are three high-symmetry stacking regions in each moiré unit cell: MM, MX and XX (M = Mo or W, X = Se or Te).

In each TMD monolayer, the band edges are located at the K or K' point of the Brillouin zone. The heterobilayer has a type-I band alignment; both the conduction and valence band edges are from MoTe₂ (ref. 11). Under zero displacement field, the valence band offset at the K or K' point between the two layers (without the moiré effect) is about 220 meV in the calculations; it is smaller than the experimental value

of about 300 meV (ref. 11). The direction of the displacement field D is chosen such that D reduces the valence band offset between the two layers. Our result illustrates the effect of the displacement field on the lowest-energy moiré valence bands. However, the absolute values of D cannot be directly compared with that of the applied electric field in the experiment.

Extended Data Figure 9 shows the moiré valence band dispersions under four representative out-of-plane displacement fields. Under zero displacement field, the top moiré valence band (red) is well separated from the rest moiré bands with a band gap of around 10 meV at the K_m point of the moiré Brillouin zone (MBZ). The two branches of the band are from the different folding scheme of the K and -K valley states, which are degenerate in energy and shifted in momentum. When the displacement field strength is increased, the single-particle band gap between the first two dispersive moiré bands at the K_m point of the MBZ (red and black lines inside the red circle) gradually closes around the critical displacement field of 0.25 V nm⁻¹; it reopens at higher fields. In addition to the dispersive moiré bands, the figures also show a flat band (blue) that intersects the low-energy dispersive moiré bands. We note that the accuracy of large-scale DFT calculations is at the meV level and the details of the single-particle band structure sensitively depend on the choice of van der Waals density functional, moiré wavelength and accuracy of the relaxed atomic coordinates even with zero filling. However, the results regarding the topological features, such as band inversion and topological Chern numbers, are robust.

We analyse the Kohn-Sham wave functions of the moiré bands in real space to identify their origin (Extended Data Figs. 8 and 9). We choose two high-symmetry points, the Γ_m point and the K_m point of the MBZ. Before gap closure (for example, $D = 0.2 \text{ V nm}^{-1}$), the wave functions of each band at the Γ_m point and the K_m point are located at the same sites of the moiré unit cell. In particular, the envelope wave function of the flat band is located at the MX site. The atomic-scale wave function consists of both the d orbitals of the M atoms and p orbitals of the X atoms; it forms a honeycomb network. This indicates that the flat band is constructed from the Γ states of the monolayer TMDs⁴⁷. The envelope wave functions of the first and second dispersive moiré bands are located at the MM site (in the MoTe₂ layer) and the XX site (in the WSe₂ layer), respectively. The atomic-scale wave functions are dominated by the d orbitals of the M atoms and form a triangular network; this indicates that the bands are developed from the K or K' states of the monolayers⁴⁷. The two topmost dispersive moiré bands thus correspond to an effective honeycomb superlattice with MM and XX sublattices.

After gap reopening, the Γ_m point wave functions of these bands remain at the same site of the moiré unit cell. However, the K_m -point wave functions of the two dispersive bands switch sites, that is, the WSe₂ moiré band near K_m now has a higher energy than the MoTe₂ moiré band. Our result demonstrates band inversion and the emergence of topological bands with finite valley-resolved Chern numbers after gap reopening. Because the envelope wave functions of the first two dispersive bands form a honeycomb lattice structure, the physics resembles the Kane–Mele model 13,23 . The displacement field tunes the potential difference between the MM and XX sites and can induce topological moiré bands. This is similar to the case of twisted TMD homobilayers, for which the Kane–Mele–Hubbard model has been proposed 21,22 .

In contrast to the 0-degree-twisted (AA-stacked) MoTe $_2$ /WSe $_2$ heterobilayers 11 , the interlayer tunnelling in AB-stacked heterobilayers is

spin-forbidden for the K or K' states in the leading-order approximation. The moiré potential is weaker and the moiré bands are more dispersive, as illustrated in Extended Data Fig. 9. The interlayer tunnelling is much stronger for the Γ states; the moiré potential is stronger and gives rise to the flat band. At charge neutrality around the critical displacement field, the flat band slightly overlaps with the first dispersive moiré band. With finite hole filling, the interaction effect renormalizes the single-particle band structure. The electrostatic repulsion from filled holes would increase the background Hartree potential and push the Γ flat band away in energy. Similarly, the moiré gap between the first two dispersive bands also increases.

Data availability

Source data are provided with this paper. All other data are available from the corresponding authors.

- Wang, L. et al. One-dimensional electrical contact to a two-dimensional material. Science 342, 614–617 (2013).
- Zibrov, A. A. et al. Tunable interacting composite fermion phases in a half-filled bilayer-graphene Landau level. Nature 549, 360–364 (2017).
- Ashoori, R. C. et al. Single-electron capacitance spectroscopy of discrete quantum levels. Phys. Rev. Lett. 68, 3088–3091 (1992).
- Xie, Y.-M., Zhang, C.-P., Hu, J.-X., Mak, K. F. & Law, K. Theory of valley polarized quantum anomalous Hall state in moiré MoTe₂/WSe₂ heterobilayers. Preprint at arXiv:2106.13991 (2021)
- Perdew, J. P., Burke, K. & Ernzerhof, M. generalized gradient approximation made simple. Phys. Rev. Lett. 77, 3865–3868 (1996).
- Peng, H., Yang, Z.-H., Perdew, J. P. & Sun, J. Versatile van der Waals density functional based on a meta-generalized gradient approximation. *Phys. Rev.* 6, 041005 (2016).
- Kresse, G. & Furthmüller, J. Efficiency of ab-initio total energy calculations for metals and semiconductors using a plane-wave basis set. Comput. Mater. Sci. 6, 15–50 (1996).
- Liu, G.-B., Xiao, D., Yao, Y., Xu, X. & Yao, W. Electronic structures and theoretical modelling of two-dimensional group-VIB transition metal dichalcogenides. *Chem. Soc. Rev.* 44, 2643–2663 (2015).

Acknowledgements This research was primarily supported by the US Department of Energy, Office of Science, Basic Energy Sciences, under award no. DE-SC0019481 (electrical measurements). The experimental study was partially supported by the Cornell Center for Materials Research with funding from the NSF MRSEC program (DMR-1719875) for device fabrication, the Air Force Office of Scientific Research under award number FA9550-19-1-0390 (capacitance measurements) and FA9550-20-1-0219 (optical characterizations), and the US Army Research Office under grant no. W911NF-17-1-0605 (analysis). The theoretical work at Massachusetts Institute of Technology was supported by the Simons Foundation through a Simons Investigator Award (theoretical analysis) and by the US Department of Energy, Office of Science, Basic Energy Sciences, Division of Materials Sciences and Engineering Awards no. DE-SC0020149 (band structure calculation). Growth of the hBN crystals was supported by the Elemental Strategy Initiative of MEXT, Japan and CREST (no. JPMJ/CR15F3), JST. This work made use of the Cornell NanoScale Facility, an NNCI member supported by NSF Grant no. NNCI-1542081. L.F. is partially supported by the David and Lucile Packard Foundation.

Author contributions T.L., S.J., B.S. and L.L. fabricated the devices, performed the measurements and analysed the data. Z.T. provided assistance with the optical characterization, Y.Z. performed the DFT calculations, Y.Z., T.D. and L.F. performed theoretical analysis. K.W. and T.T. grew the bulk hBN crystals. T.L., S.J., J.S. and K.F.M. designed the scientific objectives and oversaw the project. All authors discussed the results and commented on the manuscript.

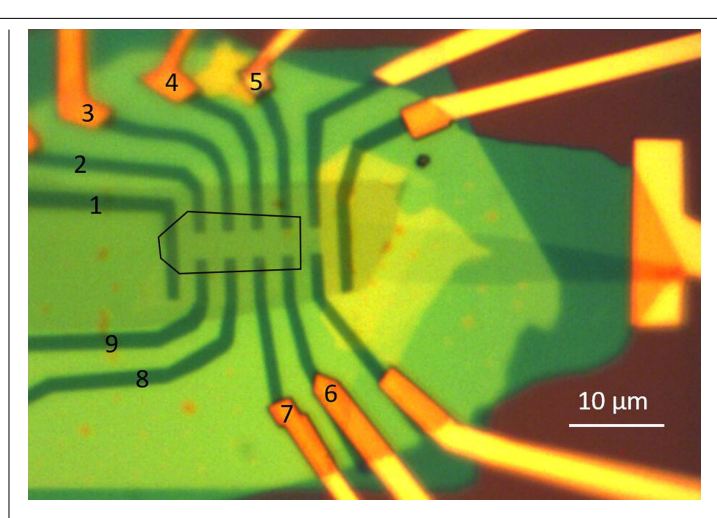
Competing interests The authors declare no competing interests

Additional information

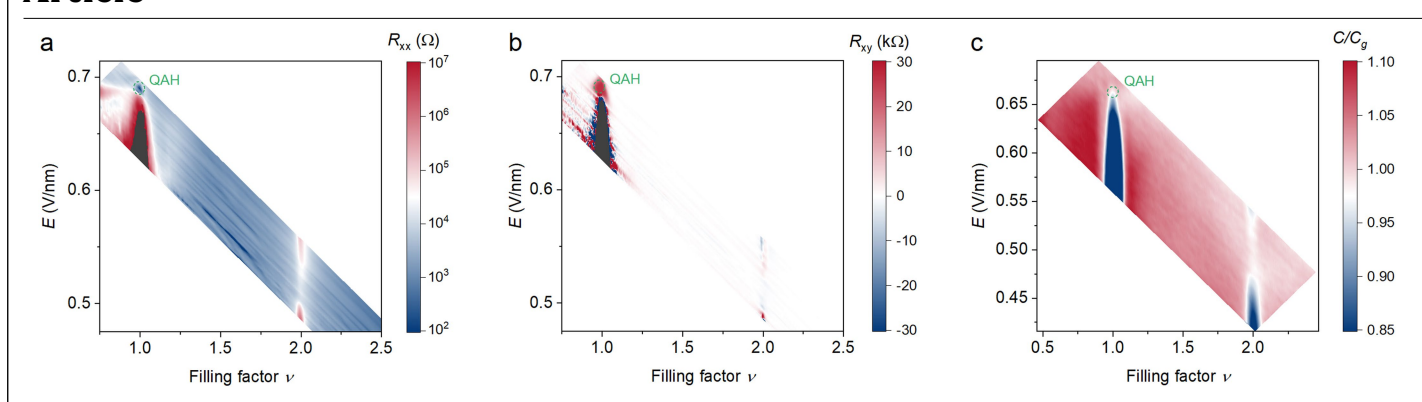
Supplementary information The online version contains supplementary material available at https://doi.org/10.1038/s41586-021-04171-1.

Correspondence and requests for materials should be addressed to Jie Shan or Kin Fai Mak. Peer review information Nature thanks Lede Xian, You Zhou and the other, anonymous, reviewer(s) for their contribution to the peer review of this work. Peer reviewer reports are available.

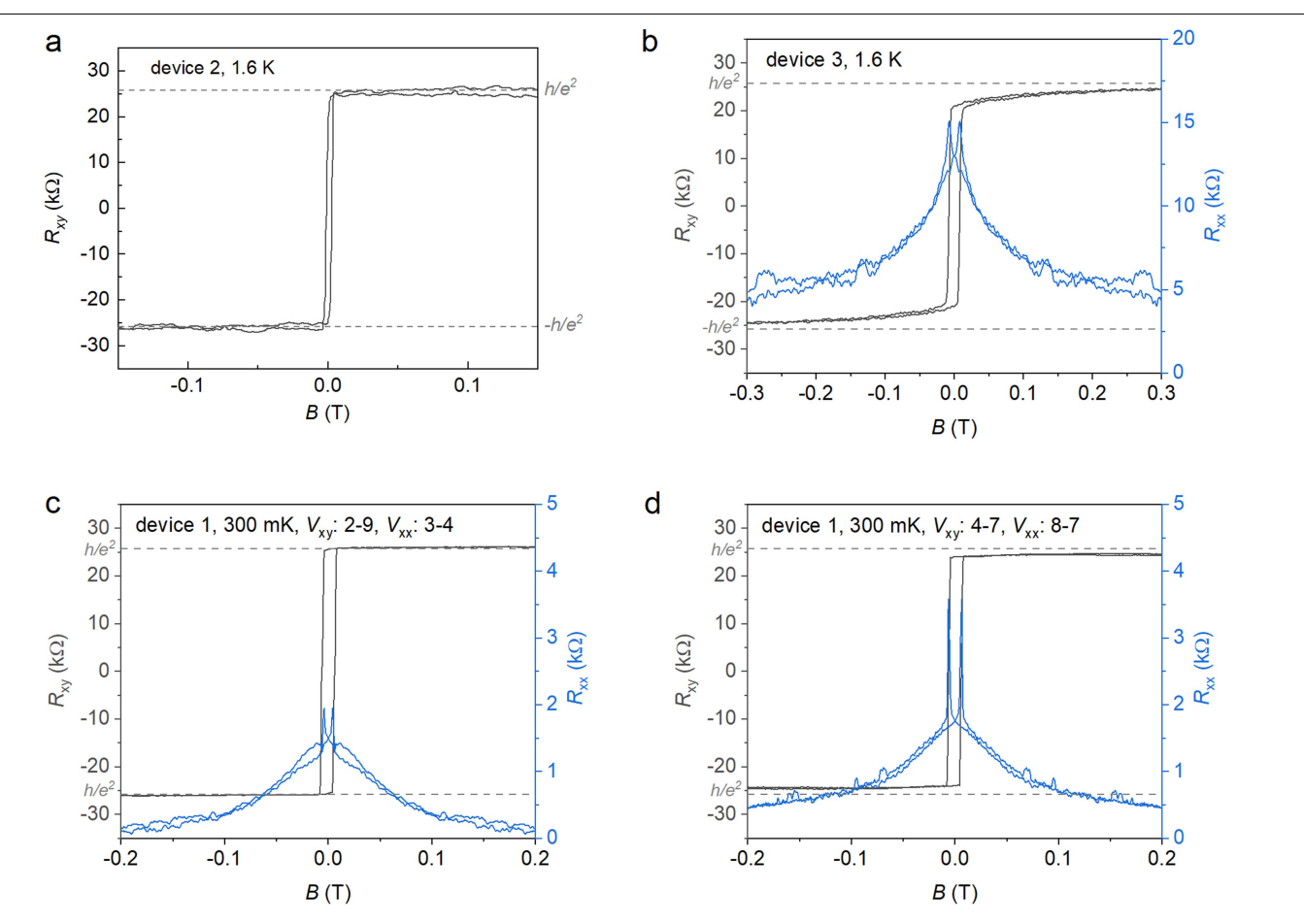
Reprints and permissions information is available at http://www.nature.com/reprints.



Extended Data Figure 1 | Optical micrograph of device 1. MoTe $_{\rm J}$ /WSe $_{\rm 2}$ heterobilayer is outlined by the black line. Electrode 1-9 are labeled. For the results presented in the main text, electrode 5 and 6 are grounded; electrode 1 is used as a source electrode. The longitudinal voltage drop is measured between 3 and 4; and the transverse voltage drop is measured between 3 and 8. The scale bar is 10 μm .

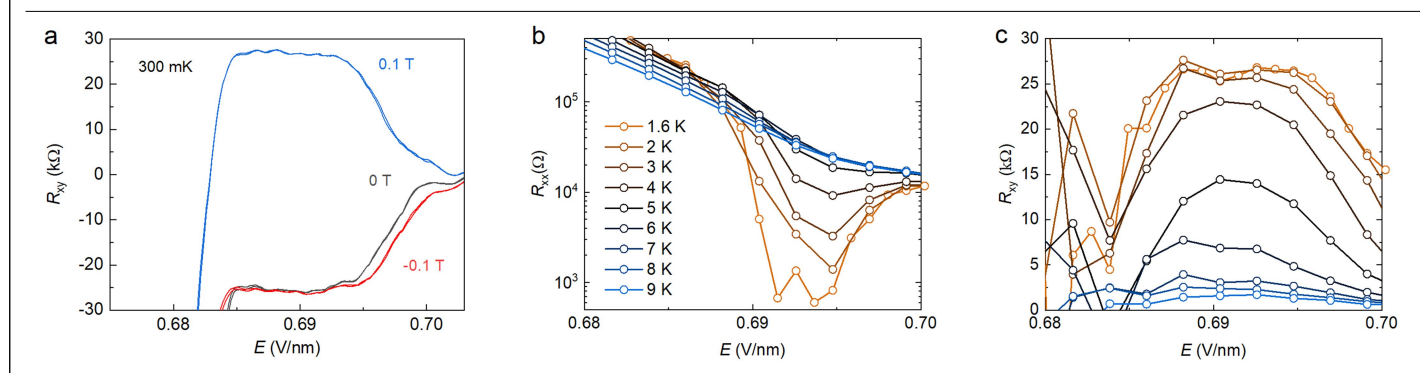


Extended Data Figure 2 | **2D maps in filling factor and electric field.** 2D map of $R_{xx}(\mathbf{a})$, $R_{xy}(\mathbf{b})$ and $C/C_g(\mathbf{c})$ as a function of filling factor and electric field. The data are converted from the 2D maps in Fig. 1c, d and 3d. The QAH region is circled by green dashed lines.



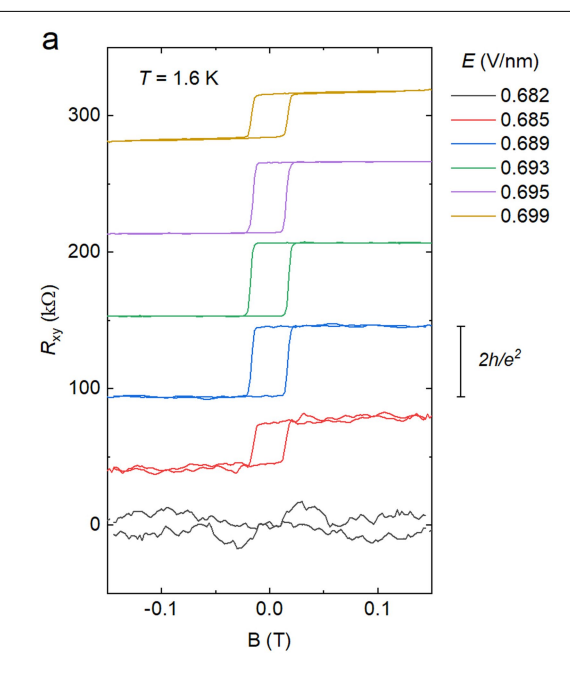
Extended Data Figure 3 | Other devices exhibiting the QAH effect at v=1. a,b, Magnetic-field dependence of R_{xy} and R_{xx} from device 2 and 3 at 1.6 K. Quantized Hall resistance at zero magnetic field is observed in device 2; R_{xx} is not measured. The resistance quantization in device 3 is nearly perfect at a small magnetic field, accompanied by a significant drop in R_{xx} . **c,d**, The same as

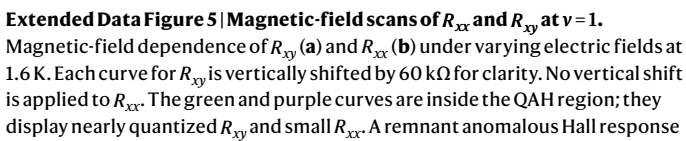
 $\begin{tabular}{ll} \textbf{a}, \textbf{b} for device 1 measured from different pairs of probes (than the result shown in the main text) at 300 mK. The labeling of the electrodes is shown in Extended Data Fig. 1. Nearly quantized resistance with similar magnetic-field dependence is observed. The coercive field varies slightly from device to device. \\\end{tabular}$

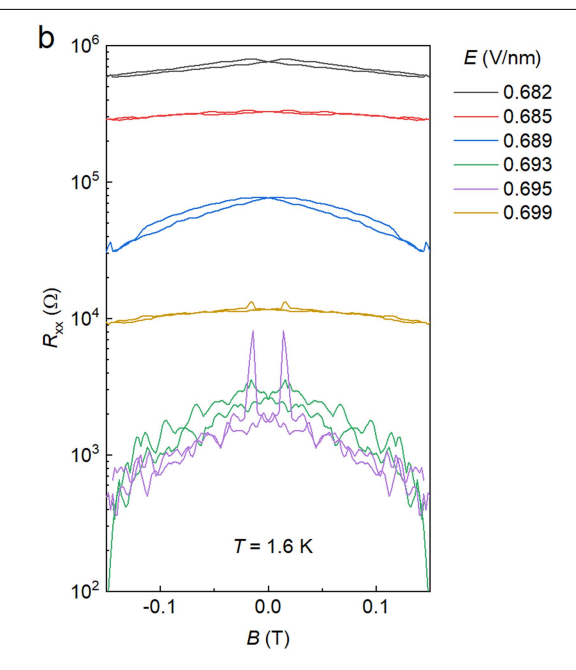


Extended Data Figure 4 | **Temperature and electric-field dependences of** R_{xx} and R_{xy} at v = 1. a, Hall resistance at v = 1 as a function of electric field under both forward and backward scans at 300 mK (device 1). The out-of-plane magnetic field is fixed at 0 or \pm 0.1T. No hysteresis is observed. Typical fluctuation of the

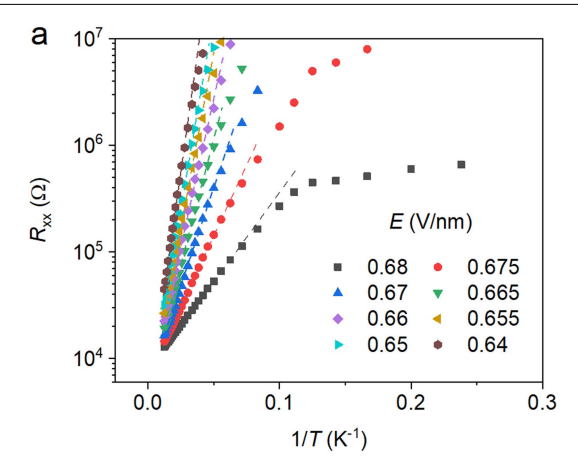
Hall plateau from the ideal value h/e^2 is about 5%. **b, c**, Electric-field dependence of R_{xx} (**b**) and R_{xy} (**c**) at varying temperatures in the zero-magnetic-field limit. A Hall plateau $R_{xy} \approx h/e^2$ in electric field, correlated with a substantial resistance dip $R_{xx} \ll R_{xy}$, is observed at low temperatures.

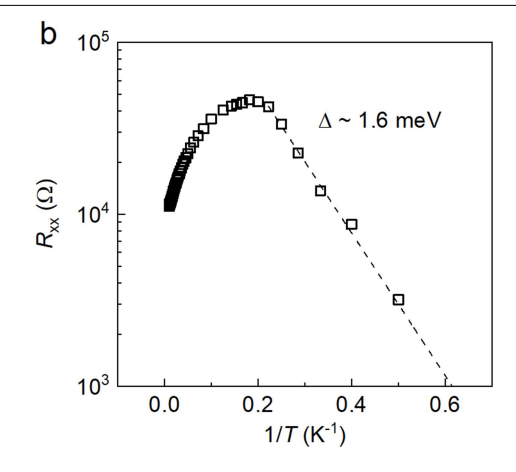






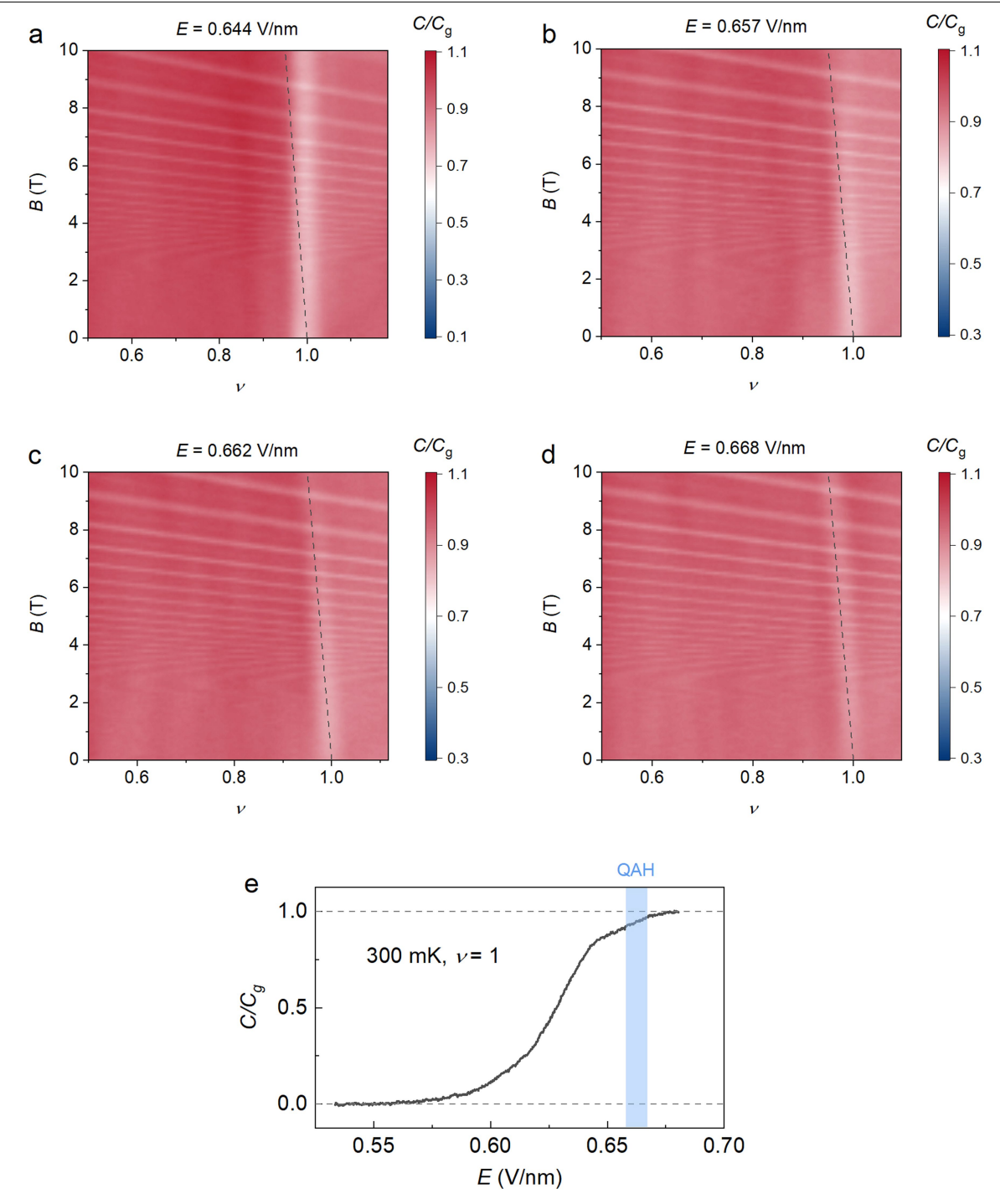
(clear magnetic hysteresis but not quantized) is observed near the QAH-metal boundary (yellow curve). A nearly quantized Hall response with large $R_{xx}\gg R_{xy}$ is observed near the Mott-QAH boundary (blue curve). It is a quantized Hall insulator. Further away from the boundary and into the Mott region, R_{xx} diverges rapidly and R_{xy} diminishes (red and black curves).





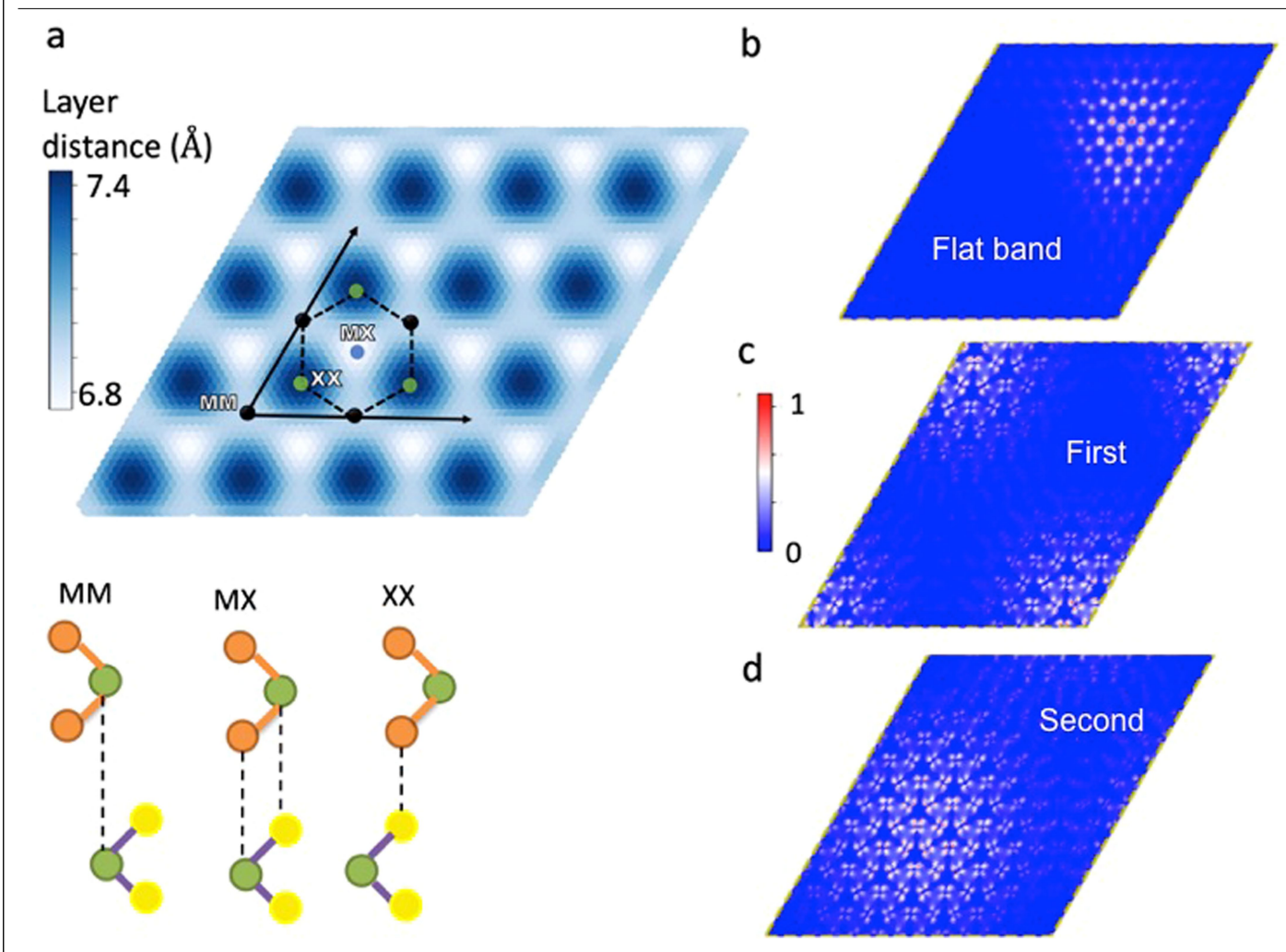
Extended Data Figure 6 | **Charge gap from thermal activation transport. a**, Arrhenius plot of R_{xx} at varying electric fields for the Mott insulator. The high-temperature data is well described by the thermal activation model (dashed lines), from which the activation gap is extracted. **b**, Same as **a** for the

QAH insulator. Here thermal activation behavior (dashed line) is observed only at low temperature, when the QAH state develops. The extracted charge gaps are shown as empty red circles (Mott insulator) and filled circle (QAH insulator) in Fig. 3c of the main text.



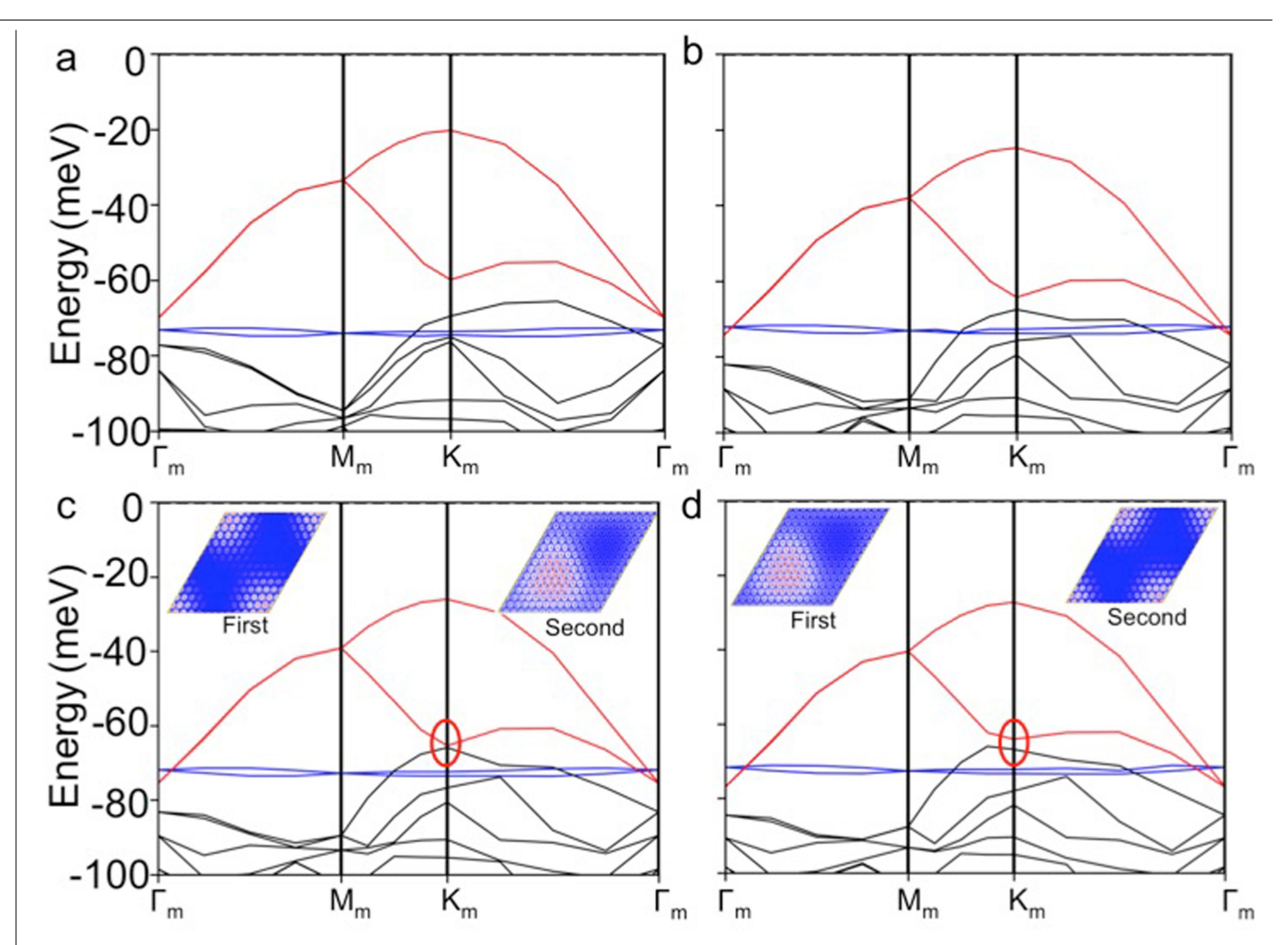
Extended Data Figure 7 | Identification of the QAH region in the capacitance device (device 6). a-d, Normalized differential top-gate capacitance, C/C_g , versus magnetic field and filling factor at 300 mK. Results for four different electric fields are shown. Most strongly dispersive incompressible states shown arise from the Landau levels of the graphite top gate and are irrelevant in this study. The black dashed lines, originated from ν = 1, are the theoretical magnetic-field dispersion of a QAH state with Chern number -1. We use this to determine the Mott-QAH insulator boundary in Fig. 3c of the main text. The system is a Mott insulator in **a** since there is no magnetic

field dispersion of the incompressible state; it is near the Mott-QAH insulator boundary in $\mathbf b$; and it is a QAH insulator in $\mathbf c$, $\mathbf d$. The QAH insulator-metal boundary is determined as capacitance reaches $C/C_g\approx 1$ in the metallic state. $\mathbf e$, Electric-field dependence of C/C_g at v=1,300 mK and zero magnetic field. The QAH region determined from $\mathbf a$ – $\mathbf d$ is shaded in blue. The normalized capacitance C/C_g equals to 1 for a metallic state at large electric fields. It is below 1 for incompressible states, which include both the Mott and QAH insulating states. Charge gap closure (i.e. $C/C_g=1$) is not observed at the Mott-QAH phase boundary.



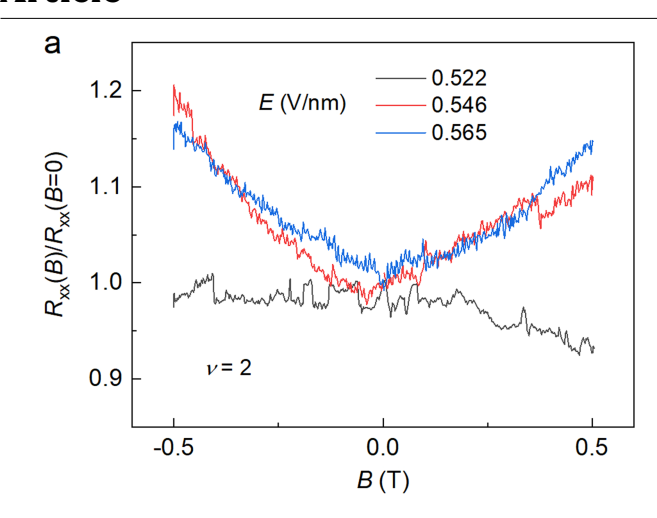
Extended Data Figure 8 | **Kohn-Sham wave functions. a**, Interlayer distance (top) and stacking alignment (bottom) of relaxed AB-stacked MoTe $_2$ /WSe $_2$ heterobilayers. MM, MX, and XX (M = Mo or W, X = Se or Te) are the high-symmetry stacking sites. **b-d**, Real-space wave function at the Γ_m -point of the MBZ for the flat band (**b**), the first (**c**) and second (**d**) dispersive valence moiré bands. The envelope wave function for the flat band is located at the MX site. The atomic-scale orbitals consist of both the d-orbitals of the M atom and

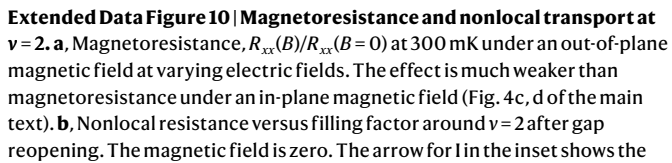
the p-orbitals of the X atom, forming a honeycomb network. The wave functions for the first and second dispersive moiré bands are located at the MM and XX sites, respectively. The atomic-scale orbitals are dominated by the d-orbitals of the M atom, forming a triangular network. The results show that the dispersive bands are originated from the K or K' valleys of the TMD monolayers.

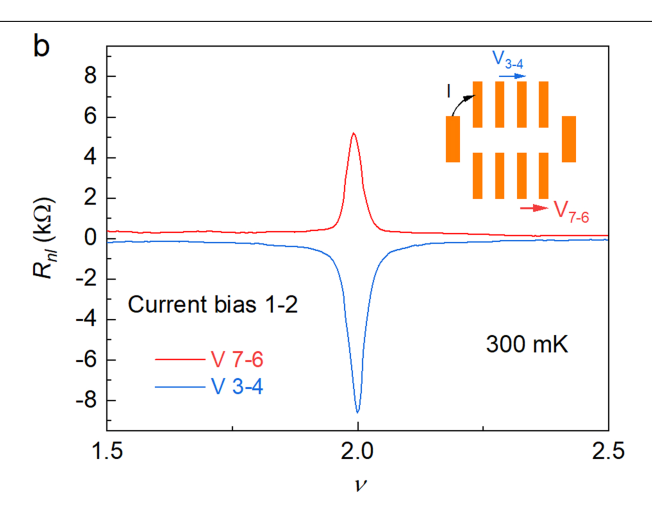


Extended Data Figure 9 | **Moiré band structure at varying displacement fields.** Moiré valence band structure of AB-stacked MoTe $_2$ /WSe $_2$ heterobilayers from DFT with displacement field 0 V/nm (a), 0.2 V/nm (b), 0.25 V/nm (c) and 0.3 V/nm (d). The first moiré band is shown in red (The two branches are from the different folding scheme of the K and –K valley states, which are degenerate in energy and shifted in momentum); the flat band is in blue; and the rest of the bands are in black. The energy gap at the K_m -point (marked by a red circle) between the two dispersive moiré bands closes and reopens between 0.25 V/nm

and 0.3 V/nm. The insets in ${\bf c}$ and ${\bf d}$ show the envelope wave function at the K_m -point of the MBZ for the first (left inset) and second (right inset) dispersive bands. Before gap closure, the K_m -point wave function for the two dispersive bands is centered at the MM and XX site, respectively. They are centered at the same sites as the Γ_m -point wave function (see Extended Data Fig. 8). The envelope wave function switches moiré sites after gap reopening, showing the emergence of topological bands (see Methods for the interaction effects).







direction of the bias electric field between the source and drain electrodes. Voltage drops between electrode 3 and 4 (V_{3-4}) and between 7 and 6 (V_{7-6}) are measured. A change in sign for the nonlocal resistance is consistent with the presence of helical edge state transport for a quantum valley-spin Hall insulator.